Effects of rotation on the rolling noise radiated by wheelsets in high-speed railways

Christopher Knuth , Giacomo Squicciarini , David Thompson , Luis Baeza

PII: S0022-460X(23)00629-6
DOI: https://doi.org/10.1016/j.jsv.2023.118180
Reference: YJSVI 118180

To appear in: *Journal of Sound and Vibration*

Received date: 3 April 2023
Revised date: 1 October 2023
Accepted date: 17 November 2023

Please cite this article as: Christopher Knuth , Giacomo Squicciarini , David Thompson , Luis Baeza , Effects of rotation on the rolling noise radiated by wheelsets in high-speed railways, *Journal of Sound and Vibration* (2023), doi: https://doi.org/10.1016/j.jsv.2023.118180

Highlights

- Extension of an existing axisymmetric finite element rotor model
- Investigation of the effects of rotation on the dynamics of a railway wheelset
- Impact of wheel rotation on rolling noise demonstrated over range of train speeds
- Results from the rotating wheelset compared with conventional model simplifications

Effects of rotation on the rolling noise radiated by wheelsets in high-speed railways

Christopher Knuth[1*], Giacomo Squicciarini[1], David Thompson[1], Luis Baeza[2]

[1] Institute of Sound and Vibration Research, University of Southampton, Southampton, UK.

[2] Instituto de Ingeniería Mecánica y Biomecánica, Universitat Politècnica de València, Valencia, Spain.

*Corresponding author: C.Knuth@soton.ac.uk

Abstract

Railway rolling noise is produced by the vibration of both the wheelsets and the track; the wheelsets dominate the high frequency noise and become increasingly important at high speed. The effect of rotation on the wheelset vibration and noise radiation is investigated using different wheelset models in a rolling noise prediction model for a wide range of speeds. Each wheelset model takes account of the rotation to a different extent. An axisymmetric finite element model of a flexible rotating wheelset is implemented based on a complex exponential formulation and expressed in either an inertial or a non-inertial frame of reference. The model can include the inertial Coriolis and centrifugal forces and is also extended to include stress stiffening. Modes of the rotating wheel with non-zero number of nodal diameters are split into co- and counter-rotating waves with separated natural frequencies. The extent of the frequency separation depends on the shape of the mode and its dominant component of vibration. At common train speeds the frequency shifts due to stress-stiffening and spin-softening effects are found to be small compared with the gyroscopic effects due to the Coriolis forces. The effect of including the inertial Coriolis and centrifugal forces on the overall A-weighted sound power level is less than 0.3 dB below 400 km/h, while for higher train speeds, differences may exceed 1 dB in some one-third octave bands. Overall, these differences are small compared with other sources of uncertainty in rolling noise modelling, confirming that representing the wheel rotation with a moving load approach provides a suitable approximation for use in rolling noise predictions.

Keywords: railways, rolling noise, rotor dynamics, Finite Elements, wheel rotation, sound radiation

1 Introduction

Rolling noise is one of the main sources of noise in modern railways and one of the major constraints in the planning of new railway routes. Railways, as a more environmentally friendly mode of travel, can play a key role in achieving the goal of becoming climate-neutral. Thus, a better understanding of the noise generation can help in finding more effective mitigation measures for railway noise and in promoting the development of new routes.

Rolling noise is produced by vibration of the wheels and the track due to roughness excitation at their surfaces; the frequency range of interest usually extends from 50 Hz to at least 5 kHz [1]. One of the most commonly used rolling noise prediction models is TWINS (Track-Wheel Interaction Noise Software) [2, 3]. This indicates that, at frequencies above 1.6 or 2 kHz, the wheel is usually the dominant source of noise.

Another aspect that should be considered in high-speed railways is the effect of the wheel rotation on the wheelset dynamics, which has only been addressed by some authors in recent decades. In the early rolling noise models by Remington [4, 5], the wheel was modelled using simple analytical models, that can only represent the non-rotating wheelset in an approximate manner. Thompson modelled the wheel using axisymmetric Finite Elements (FE) and a Fourier decomposition [6] to include the wheel resonances for different harmonics n (nodal diameters). He replaced the wheel rotation with a moving load that rotates around the wheel circumference [7]. This caused a split of the resonances (for $n > 0$) into two peaks separated by $\pm n\Omega$, where Ω is the rotational angular velocity. This approach, which is included in TWINS, neglects the inertial gyroscopic and centrifugal effects.

Two main approaches exist to formulate the equations of motion of a flexible rotating body: the Eulerian method, which makes use of an inertial (non-rotating) frame of reference that is fixed in space, and the Lagrangian method, that adopts a non-inertial (rotating) frame, where the observer is fixed to a material point on the rotor. Eulerian coordinates can be advantageous in railway applications as they allow the interaction with the track to be solved directly. Fayos et al. [8] used Eulerian coordinates to model flexible rotating structures with FE. This modelling approach has been applied in different railway applications, e.g. [9-13]. Baeza et al. [14-16] further developed both Eulerian and Lagrangian models of the rotating wheelset, allowing the use of axisymmetric elements to reduce the computational effort.

Sheng et al. [17] modelled an axisymmetric rotating wheelset including the inertial Coriolis and centrifugal forces. They found the impact of the gyroscopic effect on the

resonance frequencies to be larger than the centrifugal effect, but both effects were small compared with the moving rotating force. The model found application in several studies concerning the dynamic wheel/track interaction and noise generation [18-21].

Andrés et al. [13] recently implemented an axisymmetric Eulerian model of a rotating wheelset and applied it in rolling noise calculations. Comparisons to an equivalent 3D vibroacoustic model of a rotating wheelset implemented in commercial software showed the great benefit of these model reductions. Zhong et al. [20] coupled a rotating wheel, based on the model in [17], with an axisymmetric boundary element model and calculated the vibration and sound for a unit force input at the contact point. They found that the train speed has an impact on the power radiated from the wheel. While comparing common modelling assumptions in rolling noise calculations, Cheng et al. [21] investigated this further. Their results showed that neglecting the wheel rotation underestimates the overall sound power level by about 3 dB. However, results were only shown for a single train speed and compared with a non-rotating wheel. The relative importance of the moving load or the inertial effects were not shown. Moreover, none of the above studies considered stress-stiffening effects.

Although rotating wheel models have been presented in the literature, (e.g. [13, 21]), the influence of the various terms on the rolling noise has not been investigated over a wide range of train speeds. To give a structured assessment of this problem, this paper presents a rotating wheelset model, which can account for inertial effects and stress-stiffening, and utilizes it to quantify the changes in rolling noise spectra due to wheel rotation. The effects, on the vibration and sound radiation of the wheel, of the various terms due to rotation are investigated and the results are compared, not only with a non-rotating wheel, but also with the classical approximation of a moving load.

The remainder of this paper is structured as follows. In Section 2, the model of the rotating wheelset is developed. Section 3 presents the rolling noise model for wheel sound radiation due to roughness excitation. In Section 4, the main effects of the rotation on the wheelset dynamics are discussed. The wheelset model is used in Section 5 to calculate the radiated sound power of the wheel by accounting for the different effects of the rotation and comparing their relative importance.

2 Model of the flexible rotating wheelset

In this section, the numerical approach used to calculate the wheelset response is outlined. The Lagrangian and Eulerian approaches for modelling the rotating wheelset are adopted, based on the work of Baeza et al. [16]. The models are extended in this paper to include centrifugal stress stiffening and they are expressed as a Fourier series in terms of a complex exponential. Compared with [16], this leads to a slightly different equation of motion (EOM).

To study the effects of the inertial forces on the wheelset dynamics, a Lagrangian model is used that adopts a non-inertial reference frame **xyz**, see **Fig. 1**. For the interaction with the rail, an Eulerian model is used that adopts an inertial frame $\mathbf{x}_0\mathbf{y}_0\mathbf{z}$. In both cases, the **z**-axis is the axis of revolution of the wheelset; the wheelset is assumed to rotate at a constant angular speed Ω, i.e. the angular velocity vector is $\mathbf{\Omega} = (0,0,\Omega)^{\mathrm{T}}$. After a time t, **xyz** is shifted by an angle Ωt about the **z**-axis. At $t = 0$ and multiples of a period of revolution, the two reference frames coincide. The two approaches are described in the following.

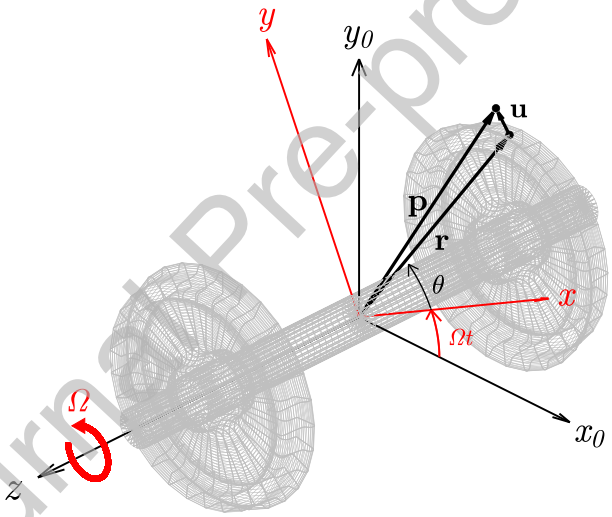

Fig. 1 Coordinate system of the flexible rotating wheelset in the Lagrangian (**xyz**) and Eulerian ($\mathbf{x}_0\mathbf{y}_0\mathbf{z}$) frames of reference.

2.1 Lagrangian model of the rotating wheelset

In the Lagrangian model, the observer is fixed in the frame that rotates with the wheelset at an angular velocity Ω. Due to the symmetry around the axis of revolution, a cylindrical coordinate system (r,θ,z) is adopted, where r is the radial, θ the circumferential and z the axial coordinate. The position **p** of a particle within the rotating vibrating structure can be decomposed by its position **r** in the undeformed configuration and a small displacement **u** due to the vibration, which is assumed to be time-harmonic. The total velocity of a particle in the non-inertial frame can be calculated as [16]

$$\mathbf{v} = \frac{\mathrm{d}\mathbf{p}}{\mathrm{d}t} = \Omega\mathbf{J}(\mathbf{r}+\mathbf{u}) + \dot{\mathbf{u}}, \tag{1}$$

which has a velocity component $\Omega\mathbf{J}(\mathbf{r}+\mathbf{u})$ due to the rigid body rotation at constant angular velocity Ω and velocity $\dot{\mathbf{u}}$ from the flexible displacement of the vibrating structure. The matrix $\mathbf{J}$ is given by [16]

$$\mathbf{J} = \begin{bmatrix} 0 & -1 & 0 \\ 1 & 0 & 0 \\ 0 & 0 & 0 \end{bmatrix}. \tag{2}$$

Using the particle velocity in Eq. (1), the kinetic energy of the rotating structure is [16]

$$\begin{aligned} T &= \frac{1}{2}\iiint_V r\rho\mathbf{v}^{\mathrm{T}}\mathbf{v}\,\mathrm{d}r\mathrm{d}\theta\mathrm{d}z \\ &= \frac{1}{2}\Omega^2\iiint_V r\rho(\mathbf{r}+\mathbf{u})^{\mathrm{T}}\mathbf{E}(\mathbf{r}+\mathbf{u})\,\mathrm{d}r\mathrm{d}\theta\mathrm{d}z + \frac{1}{2}\iiint_V r\rho\dot{\mathbf{u}}^{\mathrm{T}}\dot{\mathbf{u}}\,\mathrm{d}r\mathrm{d}\theta\mathrm{d}z \\ &+ \Omega\iiint_V r\rho\dot{\mathbf{u}}^{\mathrm{T}}\mathbf{J}(\mathbf{r}+\mathbf{u})\,\mathrm{d}r\mathrm{d}\theta\mathrm{d}z, \end{aligned} \tag{3}$$

where ρ is the density of the material, V the volume of the undeformed solid, and $\mathbf{E}$ is

$$\mathbf{E} = \mathbf{J}^{\mathrm{T}}\mathbf{J} = \begin{bmatrix} 1 & 0 & 0 \\ 0 & 1 & 0 \\ 0 & 0 & 0 \end{bmatrix}. \tag{4}$$

The total strain energy of the rotating structure, allowing for geometric non-linearity (e.g. pre-stress due to centrifugal forces [22, 23]) is

$$U = U_0 + U_g = \frac{1}{2}\iiint_V r\boldsymbol{\varepsilon}_l^{\mathrm{T}}\mathbf{D}\boldsymbol{\varepsilon}_l\,\mathrm{d}r\mathrm{d}\theta\mathrm{d}z + \iiint_V r\boldsymbol{\sigma}_0^{\mathrm{T}}\boldsymbol{\varepsilon}_{nl}\,\mathrm{d}r\mathrm{d}\theta\mathrm{d}z, \tag{5}$$

where U_0 is the strain energy of the elastic solid, U_g the geometric strain energy due to pre-stress $\boldsymbol{\sigma}_0$, $\boldsymbol{\varepsilon}_l$ contains the linear and $\boldsymbol{\varepsilon}_{nl}$ the non-linear terms of the Green-Lagrange strain tensor, and $\mathbf{D}$ is the matrix of elastic moduli. The pre-stress needs to be known prior to the calculation [22].

In the axisymmetric approach, the displacements are written as a Fourier series of spatial harmonics in the circumferential direction θ as

$$\mathbf{u}(r,\theta,z) = \sum_{n=-\infty}^{\infty}\begin{Bmatrix} u_{r,n}(r,z) \\ u_{\theta,n}(r,z) \\ u_{z,n}(r,z) \end{Bmatrix}\mathrm{e}^{\mathrm{i}n\theta} = \sum_{n=-\infty}^{\infty}\mathbf{u}_n(r,z)\mathrm{e}^{\mathrm{i}n\theta}, \tag{6}$$

where n is the harmonic order and $\mathbf{u}_n$ contains the corresponding amplitudes in radial ($u_{r,n}$), circumferential ($u_{\theta,n}$) and axial ($u_{z,n}$) directions. The displacements of harmonic n are decomposed into a forward rotating wave ($n<0$) and a backward rotating wave ($n>0$); the forward wave is co-rotating with the wheelset while the backward wave is counter-rotating. If

$n = 0$ the displacements are uniformly distributed around the wheel circumference. Equivalently, a Fourier series of sines and cosines can be adopted, as e.g. in [13, 16], but the remainder of the derivation is modified. Using Eq. (6) requires solving for negative as well as positive harmonics n but halves the required number of degrees of freedom for $n \neq 0$, compared with the formulation using sinusoids, and directly separates the solution into forward and backward rotating waves.

The kinetic energy becomes

$$\begin{aligned} T = \frac{1}{2}\Omega^2 \iiint_V r\rho \left(\mathbf{r} + \sum_{n=-\infty}^{\infty} \mathbf{u}_n \mathrm{e}^{\mathrm{i}n\theta}\right)^{\mathrm{H}} \mathbf{E} \left(\mathbf{r} + \sum_{n=-\infty}^{\infty} \mathbf{u}_n \mathrm{e}^{\mathrm{i}n\theta}\right) \mathrm{d}r\mathrm{d}\theta\mathrm{d}z \\ + \frac{1}{2} \iiint_V r\rho \left(\sum_{n=-\infty}^{\infty} \dot{\mathbf{u}}_n \mathrm{e}^{\mathrm{i}n\theta}\right)^{\mathrm{H}} \left(\sum_{n=-\infty}^{\infty} \dot{\mathbf{u}}_n \mathrm{e}^{\mathrm{i}n\theta}\right) \mathrm{d}r\mathrm{d}\theta\mathrm{d}z \\ + \Omega \iiint_V r\rho \left(\sum_{n=-\infty}^{\infty} \dot{\mathbf{u}}_n \mathrm{e}^{\mathrm{i}n\theta}\right)^{\mathrm{H}} \mathbf{J} \left(\mathbf{r} + \sum_{n=-\infty}^{\infty} \mathbf{u}_n \mathrm{e}^{\mathrm{i}n\theta}\right) \mathrm{d}r\mathrm{d}\theta\mathrm{d}z, \end{aligned} \tag{7}$$

where superscript H denotes the complex conjugate transpose, or Hermitian transpose.

The kinetic energy and strain energy are calculated numerically using the Finite Element Method. Integration over the circumferential direction can be performed analytically, as

$$\int_0^{2\pi} \mathrm{e}^{\mathrm{i}n\theta} \mathrm{e}^{\mathrm{i}m\theta} \mathrm{d}\theta = \begin{cases} 0 & \text{if } n \neq -m \\ 2\pi & \text{if } n = -m \text{ or } n = m = 0. \end{cases} \tag{8}$$

Hence, the volume integrals in the energy expressions reduce to surface integrals and only a 2D cross-section in (r, z) needs to be discretised. Applying the finite element approximation $\mathbf{u}_n \approx \mathbf{N}^e(r,z)\mathbf{u}_n^e$ and integrating over the element area A^e yields the total kinetic energy of the e-th element as

$$\begin{aligned} T^e = \frac{1}{2} \sum_{n=-\infty}^{\infty} \left(\dot{\mathbf{u}}_n^{e\,T} \mathbf{m}^e \dot{\mathbf{u}}_n^e + 2\Omega \dot{\mathbf{u}}_n^{e\,T} \mathbf{g}^e \mathbf{u}_n^e + \Omega^2 \mathbf{u}_n^{e\,T} \mathbf{b}^e \mathbf{u}_n^e\right) + \pi\Omega^2 \iint_{A^e} r\rho \mathbf{r}^{\mathrm{T}} \mathbf{E} \mathbf{r}\, \mathrm{d}r\mathrm{d}z \\ + \frac{1}{2}\Omega^2 \mathbf{u}_0^{e\,T} \mathbf{c}_0^e, \end{aligned} \tag{9}$$

where $\mathbf{N}^e(r,z)$ is the element shape function matrix consisting of 2D interpolation functions, $\mathbf{u}_n^e$ is the element displacement vector, $\mathbf{m}^e$ is the element mass matrix, $\mathbf{g}^e$ is the element gyroscopic matrix, $\mathbf{b}^e$ the element centrifugal matrix, and $\mathbf{c}_0^e$ is the element centrifugal force vector, which is constant around the circumference and only non-zero if $n = 0$. The total strain energy of the e-th element becomes

$$U^e = \frac{1}{2} \sum_{n=-\infty}^{\infty} \mathbf{u}_n^{e\,T} (\mathbf{k}_0^e + (\mathrm{i}n)\mathbf{k}_1^e + (\mathrm{i}n)^2 \mathbf{k}_2^e) \mathbf{u}_n^e + \Omega^2 \sum_{n=-\infty}^{\infty} \mathbf{u}_n^{e\,T} \mathbf{k}_g^e \mathbf{u}_n^e, \tag{10}$$

where $\mathbf{k}_0^e$, $\mathbf{k}_1^e$ and $\mathbf{k}_2^e$ are the element stiffness matrices and $\mathbf{k}_g^e$ is the element geometric stiffness matrix. The element matrices in Eqs. (9) and (10) are defined in the Appendix. The overall kinetic and strain energies are calculated by summation over the individual elements, which corresponds to the process of assembling the global matrices from the element matrices. In practice the summation over the harmonics is truncated to $n = \pm N$. The global matrices are denoted by capital letters in the rest of the formulation.

If geometric non-linearity is included ($\boldsymbol{\sigma}_0 \neq \mathbf{0}$), the static displacements $\bar{\mathbf{u}}_0$ due to the centrifugal force are calculated using the global stiffness matrix $\mathbf{K}_0$ for $n = 0$ as

$$\bar{\mathbf{u}}_0 = \Omega^2 \mathbf{K}_0^{-1} \mathbf{c}_0. \tag{11}$$

To avoid a singular $\mathbf{K}_0$, the system needs to be constrained at some degrees of freedom, e.g. at the nodes coinciding with the axis of rotation, if no other constraints are applied. From displacements $\bar{\mathbf{u}}_0$, the pre-stress $\boldsymbol{\sigma}_0$ can be calculated to obtain the elemental geometric stiffness matrix $\mathbf{k}_g^e$ (see Appendix). If $\bar{\mathbf{u}}_0$ is calculated for a unit angular velocity ($\Omega = 1$ rad/s), the element stress-stiffening matrix can be calculated for any speed as $\mathbf{k}_\Omega^e = \Omega^2 \mathbf{k}_g^e$ and assembled to the global matrix $\mathbf{K}_\Omega$.

The elemental virtual work produced by an external point force applied to the e-th element that rotates with the frame, i.e. at coordinates $(r_F, \theta = 0, z_\mathrm{F})$, can be written as follows

$$\delta W^e = \delta \mathbf{u}^e (r_F, 0, z_\mathrm{F})^\mathrm{T} \mathbf{f}^e = \sum_{n=-\infty}^{\infty} \delta \mathbf{u}_n^{e\,\mathrm{T}} \mathbf{N}^e (r_F, z_\mathrm{F})^\mathrm{T} \mathbf{f}^e, \tag{12}$$

where $\delta \mathbf{u}^e$ is the virtual displacement vector and $\mathbf{f}^e$ the vector of nodal forces applied to the element. The product $\mathbf{N}^{e\,\mathrm{T}} \mathbf{f}^e$ yields the elemental force vector which can be assembled into a global force vector by summing up the contribution on each element. If loads other than a point force are considered, another expression of the virtual work needs to be established.

Applying Lagrange's equation to the kinetic and strain energy and the virtual work yields the EOM of the Lagrangian model for harmonic $n = 0$ as

$$\mathbf{M}\ddot{\mathbf{u}}_0 + 2\Omega \mathbf{G}\dot{\mathbf{u}}_0 + (\mathbf{K}_0 + \mathbf{K}_\Omega - \Omega^2 \mathbf{B})\mathbf{u}_0 = \Omega^2 \mathbf{c}_0 + \mathbf{f}, \tag{13}$$

and for the other harmonics $n \neq 0$ as

$$\mathbf{M}\ddot{\mathbf{u}}_n + 2\Omega \mathbf{G}\dot{\mathbf{u}}_n + (\mathbf{K}_0 + (\mathrm{i}n)\mathbf{K}_1 + (\mathrm{i}n)^2 \mathbf{K}_2 + \mathbf{K}_\Omega - \Omega^2 \mathbf{B})\mathbf{u}_n = \mathbf{f}, \tag{14}$$

where $\mathbf{M}$, $\mathbf{G}$, $\mathbf{K}_0$, $\mathbf{K}_1$, $\mathbf{K}_2$, $\mathbf{K}_\Omega$, $\mathbf{B}$ are the global mass, gyroscopic, stiffness, stress-stiffening and centrifugal (or spin-softening) matrices, $\mathbf{c}_0$ is vector of the centrifugal forces that are

constant around the circumference and not causing vibration at a frequency ω, and $\mathbf{f}$ is the force vector.

In wheel/track-interaction the contact force remains at a fixed location on the wheel circumference, i.e. it is applied to the angular coordinate $\theta = -\Omega t$. The virtual work becomes

$$\delta W^e = \sum_{n=-\infty}^{\infty} \left(\delta \mathbf{u}_n^e \mathbf{N}^e(r_F, z_F) \mathrm{e}^{-\mathrm{i}n\Omega t}\right)^{\mathrm{H}} \mathbf{f}^e = \sum_{n=-\infty}^{\infty} \delta \mathbf{u}_n^{e\,\mathrm{T}} \mathbf{N}^e(r_F, z_F)^{\mathrm{T}} \mathbf{f}^e \mathrm{e}^{\mathrm{i}n\Omega t}. \tag{15}$$

The EOM of the Lagrangian model for a force applied at a fixed angular position for $n = 0$ remains the same as Eq. (13), but for any other $n \neq 0$ it becomes

$$\mathbf{M}\ddot{\mathbf{u}}_n + 2\Omega \mathbf{G}\dot{\mathbf{u}}_n + (\mathbf{K}_0 + (\mathrm{i}n)\mathbf{K}_1 + (\mathrm{i}n)^2\mathbf{K}_2 + \mathbf{K}_\Omega - \Omega^2\mathbf{B})\mathbf{u}_n = \mathbf{f}\mathrm{e}^{\mathrm{i}n\Omega t}, \tag{16}$$

in which case the frequency of the excitation is shifted by $n\Omega$.

2.2 Eulerian model of the rotating wheelset

In the Eulerian model the observer remains stationary, hence motion is perceived differently from the Lagrangian model. As the two reference frames coincide at certain times, the displacements in the Lagrangian model $\mathbf{u}$ can be related to the displacements in the Eulerian model $\mathbf{w}$ as [16]

$$\mathbf{u}(r, \theta, z) = \mathbf{w}(r, \theta + \Omega t, z), \tag{17}$$

in which case the corresponding Fourier series becomes

$$\mathbf{w}(r, \theta + \Omega t, z) = \sum_{n=-\infty}^{\infty} \begin{Bmatrix} w_{r,n}(r,z) \\ w_{\theta,n}(r,z) \\ w_{z,n}(r,z) \end{Bmatrix} \mathrm{e}^{\mathrm{i}n\theta} \mathrm{e}^{\mathrm{i}n\Omega t} = \sum_{n=-\infty}^{\infty} \mathbf{w}_n(r,z) \mathrm{e}^{\mathrm{i}n\theta} \mathrm{e}^{\mathrm{i}n\Omega t} \tag{18}$$

where $w_{r,n}$, $w_{\theta,n}$ and $w_{z,n}$ are the radial, circumferential and axial displacements.

Equation (17) allows a transformation of the displacement, velocity, and acceleration between the two frames as

$$\mathbf{u}_n = \mathbf{w}_n \mathrm{e}^{\mathrm{i}n\Omega t}, \tag{19a}$$

$$\dot{\mathbf{u}}_n = \dot{\mathbf{w}}_n \mathrm{e}^{\mathrm{i}n\Omega t} + (\mathrm{i}n\Omega)\mathbf{w}_n \mathrm{e}^{\mathrm{i}n\Omega t}, \tag{19b}$$

$$\ddot{\mathbf{u}}_n = \ddot{\mathbf{w}}_n \mathrm{e}^{\mathrm{i}n\Omega t} + 2(\mathrm{i}n\Omega)\dot{\mathbf{w}}_n \mathrm{e}^{\mathrm{i}n\Omega t} + (\mathrm{i}n\Omega)^2 \mathbf{w}_n \mathrm{e}^{\mathrm{i}n\Omega t}. \tag{19c}$$

Considering the case with the force that is fixed in space, after substituting Eqs. (19a) – (19c) into the Lagrangian EOM given by Eqs. (13) and (16), the Eulerian EOM for harmonic $n = 0$ can be written as

$$\mathbf{M}\ddot{\mathbf{w}}_0 + 2\Omega\mathbf{G}\dot{\mathbf{w}}_0 + (\mathbf{K}_0 + \mathbf{K}_\Omega - \Omega^2\mathbf{B})\mathbf{w}_0 = \Omega^2\mathbf{c}_0 + \mathbf{f}, \tag{20}$$

and for any other harmonic $n \neq 0$ it is

$$\begin{aligned}\mathbf{M}\ddot{\mathbf{w}}_n + 2\Omega(\mathbf{G} + (\mathrm{i}n)\mathbf{M})\dot{\mathbf{w}}_n \\ + \left(\mathbf{K}_0 + (\mathrm{i}n)\mathbf{K}_1 + (\mathrm{i}n)^2\mathbf{K}_2 + \mathbf{K}_\Omega - \Omega^2(\mathbf{B} - 2(\mathrm{i}n)\mathbf{G} - (\mathrm{i}n)^2\mathbf{M})\right)\mathbf{w}_n \\ = \mathbf{f}.\end{aligned} \tag{21}$$

The difference in the observed frequency when changing between the two frames of reference can be seen by comparing their vibration as

$$\mathbf{w}_n \mathrm{e}^{\mathrm{i}\omega_E t} = \mathbf{u}_n \mathrm{e}^{-\mathrm{i}n\Omega t}\mathrm{e}^{\mathrm{i}\omega_L t} = \mathbf{u}_n \mathrm{e}^{\mathrm{i}(\omega_L - n\Omega)t}, \tag{22}$$

where $\omega_E = \omega_L - n\Omega$ is the circular frequency perceived in the Eulerian frame, and ω_L the circular frequency in the Lagrangian frame. Hence, a backward wave ($n > 0$) in the inertial frame is observed at a lower frequency and a forward wave ($n < 0$) is observed at a higher frequency compared with the non-inertial frame.

2.3 Solving the equation of motion

The Eulerian and Lagrangian models can be solved using similar methods to obtain the free and forced response in the inertial or non-inertial frame, respectively. To solve the EOM, time-harmonic motion at a circular frequency ω is assumed, such $\mathbf{f} = \hat{\mathbf{f}}\mathrm{e}^{\mathrm{i}\omega t}$and $\mathbf{u}_n = \hat{\mathbf{u}}_n \mathrm{e}^{\mathrm{i}\omega t}$ (Lagrangian) or $\mathbf{w}_n = \hat{\mathbf{w}}_n \mathrm{e}^{\mathrm{i}\omega t}$ (Eulerian). For harmonic n, the Eulerian EOM given by Eqs. (20) and (21) becomes

$$(-\omega^2\mathbf{M} + \mathrm{i}\omega 2\Omega\mathbf{G}_n + \mathbf{K}_0 + (\mathrm{i}n)\mathbf{K}_1 + (\mathrm{i}n)^2\mathbf{K}_2 + \mathbf{K}_\Omega - \Omega^2\mathbf{B}_n)\hat{\mathbf{w}}_n = \hat{\mathbf{f}}, \tag{23}$$

where $\mathbf{G}_n$ includes the inertial terms related to Ω and $\mathbf{B}_n$ the ones related to Ω^2, and $\hat{\mathbf{w}}_n$ is the vector of displacement amplitudes. Similarly, the Lagrangian EOM given by Eqs. (13) and (14) can be solved for the displacements $\hat{\mathbf{u}}_n$ and the natural frequencies in the non-inertial frame (here: $\mathbf{G}_n$ and $\mathbf{B}_n$ are identical to $\mathbf{G}$ and $\mathbf{B}$ for all n).

A modal expansion can be applied as $\hat{\mathbf{w}}_n = \boldsymbol{\phi}_n\tilde{\mathbf{w}}_n$, using the mode shapes $\boldsymbol{\phi}_n$ of harmonic n of the non-rotating solid as the basis, with $\tilde{\mathbf{w}}_n$ representing the modal amplitudes. To calculate $\boldsymbol{\phi}_n$, the eigenvalue problem for $\Omega = 0$ is solved for each harmonic n. After pre-multiplying with $\boldsymbol{\phi}_n^{\mathrm{H}}$, the EOM in modal coordinates becomes

$$\left(-\omega^2\tilde{\mathbf{M}} + \mathrm{i}\omega\left(\tilde{\mathbf{C}}_n + 2\Omega\tilde{\mathbf{G}}_n\right) + \tilde{\mathbf{K}}_n - \Omega^2\tilde{\mathbf{B}}_n\right)\tilde{\mathbf{w}}_n = \boldsymbol{\phi}_n^{\mathrm{H}}\hat{\mathbf{f}}, \tag{24}$$

where $\widetilde{\mathbf{M}}$ is the modal mass, $\widetilde{\mathbf{K}}_n$ the modal stiffness, $\widetilde{\mathbf{G}}_n$ the modal gyroscopic, $\widetilde{\mathbf{B}}_n$ the modal centrifugal matrix and $\boldsymbol{\phi}_n^{\mathrm{H}}\hat{\mathbf{f}}$ is the modal force vector. A modal damping matrix $\tilde{\mathbf{C}}_n$ can be included with terms

$$\tilde{c}_{n,ij} = 2\xi_n\sqrt{m_{ij}k_{n,ij}}, \tag{25}$$

where ξ_n is the modal damping ratio for modes at harmonic n, m_{ij} and $k_{n,ij}$ are the i,j-th elements of the modal mass and stiffness matrices. Any rotor damping that depends on Ω or higher orders of Ω (see [23, 24]) is not included in the formulation.

The free response for harmonic n is obtained by setting $\tilde{\mathbf{C}}_n = \mathbf{0}$ and $\hat{\mathbf{f}} = \mathbf{0}$ and re-writing the second-order eigenvalue problem as a linear eigenvalue problem in $\lambda = \mathrm{i}\omega$ as [24]

$$\left(\lambda\begin{bmatrix} 2\Omega\widetilde{\mathbf{G}}_n & \widetilde{\mathbf{M}} \\ \widetilde{\mathbf{M}} & \mathbf{0} \end{bmatrix} + \begin{bmatrix} \widetilde{\mathbf{K}}_n - \Omega^2\widetilde{\mathbf{B}}_n & \mathbf{0} \\ \mathbf{0} & -\widetilde{\mathbf{M}} \end{bmatrix}\right)\begin{Bmatrix} \widetilde{\mathbf{w}}_n \\ \dot{\widetilde{\mathbf{w}}}_n \end{Bmatrix} = \mathbf{0}. \tag{26}$$

The forced response for harmonic n is obtained by inverting the modal dynamic stiffness matrix and converting the displacements from the modal to the physical domain as

$$\widehat{\mathbf{w}}_n = \boldsymbol{\phi}_n\left(-\omega^2\widetilde{\mathbf{M}} + \mathrm{i}\omega\left(\tilde{\mathbf{C}}_n + 2\Omega\widetilde{\mathbf{G}}_n\right) + \widetilde{\mathbf{K}}_n - \Omega^2\widetilde{\mathbf{B}}_n\right)^{-1}\boldsymbol{\phi}_n^{\mathrm{H}}\hat{\mathbf{f}}. \tag{27}$$

For the non-rotating wheel, Ω is set to 0 and the EOM is solved as

$$\widehat{\mathbf{w}}_n = \boldsymbol{\phi}_n\left(-\omega^2\widetilde{\mathbf{M}} + \mathrm{i}\omega\tilde{\mathbf{C}}_n + \widetilde{\mathbf{K}}_n\right)^{-1}\boldsymbol{\phi}_n^{\mathrm{H}}\hat{\mathbf{f}}. \tag{28}$$

If the rotation is replaced with a moving load $\tilde{\mathbf{f}}$ that rotates in the opposite direction around the perimeter of the non-rotating wheel ($\tilde{\mathbf{f}} = \hat{\mathbf{f}}\mathrm{e}^{\mathrm{i}n\Omega t}$), as in [7], the forced vibration in the presented model with the non-rotating frame is solved as follows

$$\widehat{\mathbf{w}}_n = \boldsymbol{\phi}_n\left(-(\omega + n\Omega)^2\widetilde{\mathbf{M}} + \mathrm{i}(\omega + n\Omega)\tilde{\mathbf{C}}_n + \widetilde{\mathbf{K}}_n\right)^{-1}\boldsymbol{\phi}_n^{\mathrm{H}}\tilde{\mathbf{f}}, \tag{29}$$

where ω is replaced by $\omega + n\Omega$, while for $n = 0$ the response is identical to the non-rotating wheel.

3 Sound radiation of the railway wheel in rolling noise predictions

The sound power produced by the wheelset is calculated using the procedure adopted in TWINS [2, 3], but using the vibration of the rotating wheelset model from Section 2 as an input. The rolling noise component of the wheel is evaluated, while the track model is solely used here to determine the contact forces.

3.1 Interaction of the wheel and the track

The mobilities of the rotating wheel are obtained from the Eulerian model, including the inertial effects due to the rotation. Additionally, a non-rotating wheel, and a rotating wheel that is approximated by a moving load are implemented for comparison. A Young's modulus of $E = 2.1$ GPa, a Poisson ratio of $\nu = 0.3$, and a density of $\rho = 7850$ kg/m^3 are used. The modal damping ratios from [1] were adopted, which are $\xi_n = 10^{-3}$ for $n = 0$, $\xi_n = 10^{-2}$ for $|n| = 1$, and $\xi_n = 10^{-4}$ for $|n| \geq 2$. The mobilities are calculated for a frequency spacing of 0.1 Hz, as suggested in [1, 21]. This was sufficient to ensure at least 2-3 frequency points occur within the half-power bandwidth of the lightly damped resonances at the relevant frequencies and to capture the antiresonances of the wheelset.

The track mobilities are calculated using an infinite Timoshenko beam model with equivalent continuous support consisting of a spring-mass-spring system to represent the rail pad and a half sleeper embedded in ballast [1, 25]. The vertical and lateral mobilities are solved separately, and the vertical/lateral coupling is introduced as a scaled geometric average [2]. Damping is included in the rail, the rail pad, and the ballast in the form of a complex stiffness. The track parameters used are listed in **Table 1**.

The mobility of the contact zone is represented by a linearized Hertzian spring, see e.g. [1], for a normal load of 50 kN per wheel. The wheel and rail are coupled through the lateral creep forces and contact stiffness, see [1, 26]. For simplicity, a combined roughness spectrum is adopted that corresponds to the limit in ISO 3095 [27]. A contact filter derived using the discrete point reacting springs (DPRS) method [28] is adopted.

Table 1 Track parameters used in the model

Parameter	Vertical	Lateral
Rail bending stiffness	6.42 MNm^2	1.07 MNm^2
Rail mass per unit length	60 kg/m	
Rail shear stiffness	617 MN	
Rail shear coefficient	0.40	
Rail rotational inertia	0.24 kgm	0.04 kgm
Rail damping loss factor	0.02	
Rail pad stiffness	250 MN/m	50 MN/m

Rail pad damping loss factor	0.20	
Sleeper mass (half sleeper)	140 kg	
Ballast stiffness (half sleeper)	200 MN/m	35 MN/m
Ballast damping loss factor	1	2
Support spacing	0.60 m	

The wheel/track interaction is solved in the frequency domain for the coupled vertical (radial in the wheel) and lateral (axial in the wheel) degrees of freedom to obtain the respective contact forces for a vertical roughness input as [1]

$$\mathbf{f}_c = [\mathbf{Y}_w + \mathbf{Y}_r + \mathbf{Y}_c]^{-1} \begin{Bmatrix} \mathrm{i}\omega R \\ 0 \end{Bmatrix}, \tag{30}$$

where $\mathbf{Y}_w$, $\mathbf{Y}_r$ and $\mathbf{Y}_c$ are the wheelset, rail and contact mobility matrices (each of size 2×2 at each frequency to include vertical, lateral, and cross mobilities), and R is the roughness amplitude.

3.2 Wheel response and sound radiation

The contact forces are now used to calculate the wheel vibration in the radial and axial directions for each harmonic n in the non-rotating frame as [1]

$$\dot{\mathbf{w}}_n = \mathbf{Y}_{n,w} \mathbf{f}_c, \tag{31}$$

where $\mathbf{Y}_{n,w}$ is the mobility matrix of the wheel at harmonic n. In the non-rotating frame (Eulerian model), roughness at a certain frequency ω will excite both forward and backward waves of a given mode at the same frequency, whereas in a rotating frame (Lagrangian model), the roughness will excite the two waves at different frequencies $\omega \pm |n|\Omega$ [1].

The circumferential mean square velocity of the rotating wheel for each harmonic can be calculated analytically, see Eq. (8), by averaging of the mean square responses of the radial ($\overline{\dot{w}_{r,n}^2}$) and axial ($\overline{\dot{w}_{z,n}^2}$) component over θ as

$$\langle \overline{\dot{w}_{i,n}^2} \rangle = \frac{1}{2\pi} \int_{-\pi}^{\pi} \overline{\dot{w}_{i,n}^2} \, \mathrm{d}\theta = \frac{1}{2\pi} \int_{-\pi}^{\pi} \frac{\left(\dot{w}_{i,n} \mathrm{e}^{\mathrm{i}n\theta}\right)^* \dot{w}_{i,n} \mathrm{e}^{\mathrm{i}n\theta}}{2} \mathrm{d}\theta = \frac{\left|\dot{w}_{i,n}\right|^2}{2}, \tag{32}$$

where $\langle \overline{\ } \rangle$ denotes the spatial and temporal average and * the complex conjugate, with subscript i referring to the radial ($i = r$) and axial ($i = z$) velocity components. As the rotating waves do not have fixed nodal lines, the circumferential averaged response is identical to the mean square response at the driving point [1]. For each $n \neq 0$ of the rotating wheel, the response of the pair of harmonics $\pm n$ is added as

$$\overline{\langle \dot{w}_{i,n}^2 \rangle} = \frac{\left|\dot{w}_{i,+n}^2\right|^2}{2} + \frac{\left|\dot{w}_{i,-n}^2\right|^2}{2}. \tag{33}$$

When rotation is included, waves with $+n$ have different resonance frequencies than the waves with $-n$. Thus their resonance peaks occur at a different frequency and there will not be a simple formation of standing waves [1].

For a non-rotating wheel, for $n \neq 0$, the waves of both harmonics $+n$ and $-n$ have the same resonance frequency and are simultaneously excited by the contact force. They combine and form a standing wave, so the combined response is written as

$$\begin{aligned} \dot{w}_{i,n} &= \dot{w}_{i,-n} e^{-\mathrm{i}n\theta} + \dot{w}_{i,+n} e^{+\mathrm{i}n\theta} \\ &= \left(\dot{w}_{i,-n} + \dot{w}_{i,+n}\right)\cos(n\theta) + \mathrm{i}\left(\dot{w}_{i,+n} - \dot{w}_{i,-n}\right)\sin(n\theta), \end{aligned} \tag{34}$$

which results in a standing wave with a symmetric cosine and an antisymmetric sine component, as in the classic axisymmetric approach of non-rotating structures [22, 29]. Only the symmetric component is excited by vertical and lateral forces. The circumferential mean square velocity of each nodal diameter $n \neq 0$ becomes

$$\overline{\langle \dot{w}_{i,n}^2 \rangle} = \frac{1}{2\pi}\int_{-\pi}^{\pi} \frac{\dot{w}_{i,n}{}^{*}\dot{w}_{i,n}}{2}\cos^2(n\theta)\,\mathrm{d}\theta = \frac{\left|\left(\dot{w}_{i,-n} + \dot{w}_{i,+n}\right)\right|^2}{4}, \tag{35}$$

while for $n = 0$ the circumferential mean square is identical to Eq. (32). By combining the harmonics, in subsequent calculations the response can be expressed as a sum over the nodal diameters from $n = 0$ to $n = +N$.

In this study, the comparison between different modelling approaches is made in terms of the sound power. For calculating the radiated sound power of the wheel, the approximate radiation efficiencies from [30] are adopted for each nodal diameter n for radial and axial normal velocities. The total radiated sound power is obtained by summing up the contributions over all harmonics as

$$W = \sum_{n=0}^{N} \rho_0 c_0 \left(\sigma_{r,n}\overline{\langle \dot{w}_{r,n}^2 \rangle} S_r + \sigma_{z,n}\overline{\langle \dot{w}_{z,n}^2 \rangle} S_z\right), \tag{36}$$

where $\sigma_{r,n}$ is the radiation efficiency of the wheel for radial vibration and $\sigma_{z,n}$ for axial vibration at the nodal diameter n, $\overline{\langle \dot{w}_{r,n}^2 \rangle}$ is the circumferential mean square velocity of the radial and $\overline{\langle \dot{w}_{z,n}^2 \rangle}$ of the axial vibration at n and averaged over a number of wheel nodes, S_r and S_z are the respective radiating surface areas, ρ_0 and c_0 are the density and the speed of sound of air, with $\rho_0 = 1.2$ kg/m^3 and $c_0 = 343$ m/s. The sound radiation from the axle is not included in this approach.

4 Effect of the wheel rotation on its vibration

Before using the rotating wheel model for rolling noise calculations, the effects of the rotation on its modes of vibration are discussed. The Lagrangian model is used for the free vibration studies. Train speeds from 0 to 500 km/h are considered. This corresponds to a maximum angular velocity of 319 rad/s or a rotational frequency of 51 Hz (revolutions per second) for the wheel model with a radius of 43.5 cm at the nominal contact point, that was used in the studies.

4.1 Effect of the rotation on the wheel modal frequencies

To study the effect of the rotation on the modal frequencies, a single wheel with a straight web is modelled with the proposed FE model. The wheel is constrained at the inner radius of the hub, to account for the connection to the axle. When adding the rigid body motion, this is a good approximation of the full wheelset at frequencies where rolling noise from the wheels becomes dominant [1]. Second order elements with quadratic shape functions are used in the FE model and a mesh with a maximum element size of 1 cm is adopted, which is fine enough to represent the modes at the highest frequency of interest in the calculations.

4.1.1 Gyroscopic and centrifugal effects

The gyroscopic and centrifugal effects due to the inertial Coriolis (**G**) and centrifugal (**B**) terms are a result of changes in the kinetic energy when adding the rotation. Both effects are considered in the calculations presented here. Stress stiffening, which is due to changes in the strain energy, is analysed separately in Section 4.1.2; hence the stress-stiffening matrix is set to $\mathbf{K}_{\Omega} = \mathbf{0}$ here.

Fig. 2 shows the frequency shifts in the non-inertial frame for some example modes that are predominantly radial (a), circumferential (b), and axial (c). Note that in railway wheels there is always some coupling of vibration in different directions. As a result, modes that predominantly vibrate in one direction also exhibit by some vibration in the other two. Modes for harmonics between $n = -5$ and $n = 5$ but excluding $n = 0$, are included in the figure. The axial modes include modes with 0, 1 and 2 nodal circles. A positive value of frequency shift denotes an increase of the natural frequency compared with the non-rotating wheel. The modes are distinguished between forward ($n < 0$, dashed line) and backward rotating modes ($n > 0$, dotted line). The maximum expected shift of $\pm\Omega/2\pi$ (solid line) due to Coriolis forces is shown for comparison.

The radial modes can have a frequency split that is almost as large as $\pm\Omega/2\pi$ because they produce large Coriolis forces. The Coriolis force acting on a rotating and vibrating particle of

mass m is defined by the cross-product $\mathbf{f}_{\mathrm{Cor}} = -2m(0,0,\Omega)^{\mathrm{T}} \times (\dot{u}_r, \dot{u}_\theta, \dot{u}_z)^{\mathrm{T}}$. Hence, Coriolis forces are only produced if the structural vibration has components perpendicular to the angular velocity vector **Ω.** This is the case for radial ($\dot{u}_r$) or circumferential ($\dot{u}_\theta$) velocities. Consequently, a purely radial velocity would result in $\mathbf{f}_{\mathrm{Cor}} = -2m\Omega(0, \dot{u}_r, 0)^{\mathrm{T}}$. For the radial modes, if observed from the non-inertial frame, the forward rotating wave decreases in frequency, while the backward rotating wave increases [16, 24].

For the circumferential modes, the frequency shift is similar to the radial ones, but conversely to radial modes, the forward modes increase in frequency, while backward modes decrease. The Coriolis force $\mathbf{f}_{\mathrm{Cor}} = 2m\Omega(\dot{u}_\theta, 0,0)^{\mathrm{T}}$ for a purely circumferential velocity inverts the frequency shift of the two waves.

In general, the lower order radial and circumferential modes tend to shift in frequency more than the higher order ones; the largest shifts are seen for $n = 1$ and $n = 2$. That occurs because the higher order modes have shorter structural wavelengths in the circumferential direction, which means there is more circumferential motion in the radial modes and vice versa.

The axial modes generally have the smallest frequency shift, with the largest difference at around 25% of the maximum expected $\pm\Omega/2\pi$. A purely axial velocity ($\dot{u}_z$) would not produce any Coriolis forces when the wheel is rotating, i.e. $\mathbf{f}_{\mathrm{Cor}} = (0,0,0)^{\mathrm{T}}$. However, due to the coupling between the axial vibration and vibration in the other two directions, there is still some frequency shift in the axial modes. The shift depends on whether the coupling is stronger with radial or circumferential vibration. In the considered harmonics, axial modes with 0-nodal and 1-nodal circles shift in the same direction as the radial modes, whereas the 2-nodal-circle modes shift in the same direction as the circumferential ones.

In all cases, the inertial centrifugal effects due to the spin-softening matrix **B** lead to negligible frequency shifts in the range of train speeds considered. They are not separately shown here but they have been found to be less than 1 Hz, which is in line with [17]. Due to the Ω^2-dependency, the reduction in stiffness or natural frequency, also referred to as spin softening, may become more significant at very high angular velocities. This can be the case in other rotor dynamics applications such as turbomachinery, but a noticeable effect is not reached in conventional high-speed railways.

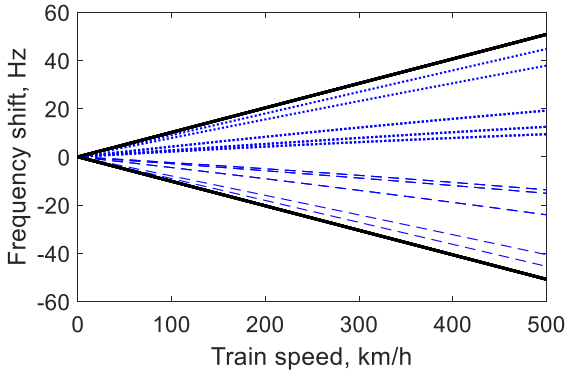

(a)

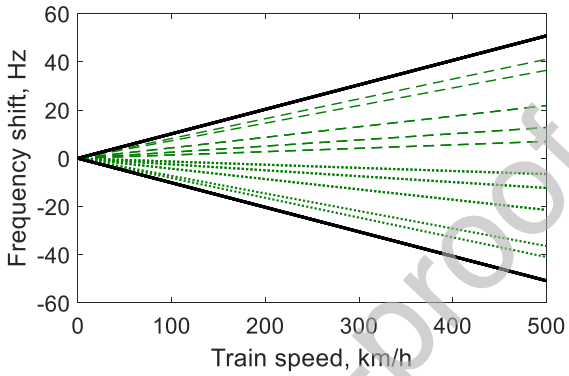

(b)

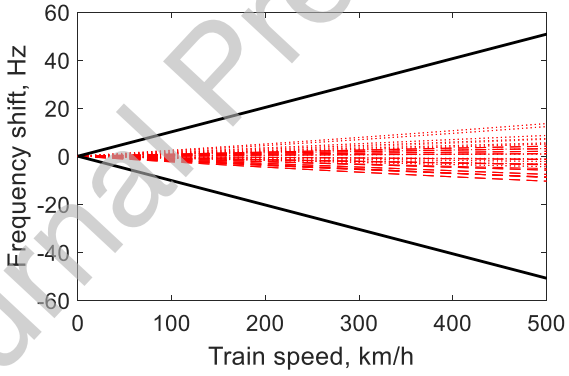

(c)

Fig. 2 Frequency shift in the non-inertial frame for different types of modes of the rotating wheel up to train speeds of 500 km/h separated between (a) radial, (b) circumferential and (c) axial modes; – – –, forward rotating wave; · · ·, backward rotating wave; ▬, $\pm\Omega/2\pi$.

4.1.2 Effect of stress stiffening

The stress-stiffening effect on different mode types is investigated by including the stress-stiffening matrix $\mathbf{K}_\Omega$ in the Lagrangian EOM, as well as the spin-softening matrix **B**. The gyroscopic effect that causes the split of the modes is excluded by setting $\mathbf{G} = \mathbf{0}$.

In **Fig. 3**, the frequency shift due to stress stiffening and spin softening is shown for the same modes as in **Fig. 2** (note the different scale). The stress-stiffening effect is largest for axial modes. It increases the natural frequencies of both the forward and backward modes

almost identically at the tested train speeds. Stress stiffening changes the bending stiffness of the wheel because of the constant centrifugal force $\mathbf{c}_0$ that acts in the radial direction. Consequently, modes with a dominant axial out-of-plane vibration can be affected whereas radial or circumferential modes are less sensitive to this phenomenon.

The calculations performed show that, even for axial modes, the effect of stress stiffening is small. The maximum frequency increase is only about 10 Hz, or 20% of the rotational frequency $\Omega/2\pi$, at a speed of 500 km/h. At more realistic speeds of a modern high-speed train (up to 350 km/h) it is at most 5 Hz.

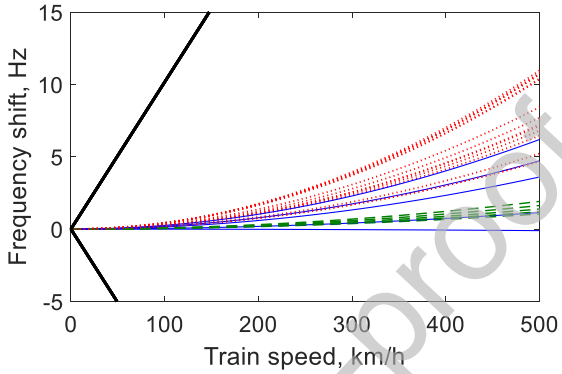

Fig. 3 Frequency shift due to centrifugal stress stiffening for train speeds up to 500 km/h on different types of wheel modes; —, radial modes; – – –, circumferential modes; · · ·, axial modes; ▬, $\pm\Omega/2\pi$.

4.1.3 Estimating the natural frequencies in the inertial frame

For the interaction with the track, the modal frequencies of the rotating waves $\omega_{m,n}$ are required in the inertial frame of reference, i.e. by using Eulerian coordinates. The lowest critical speed of the studied wheel is reached if the train travels at a speed of 1836 km/h (591 km/h for the case of the full wheelset considered below). Below this train speed, the angular velocity Ω of the wheel is smaller than the speed $\omega_{m,n}/(-n)$ of the rotating waves with $n \neq 0$. As Ω is subcritical for all modes in the considered range of train speeds, the forward and backward waves retain their direction of rotation when observed in the inertial frame [16].

The modal frequencies in the inertial frame can be obtained directly using the Eulerian model or by solving the Lagrangian model and converting them to the inertial frame. Alternatively, one could estimate them approximately from a non-rotating model. The results in Sections 4.1.1 and 4.1.2 showed that many axial modes barely change their frequency due to gyroscopic or centrifugal effects, while the radial forward waves decrease by up to $-\Omega$ and the backward waves increase by up to $+\Omega$ in circular frequency. For the circumferential modes the shifts are in the opposite direction to the radial ones. Assuming purely radial or

circumferential modes, the shifts from the gyroscopic and centrifugal effects are $\mp\Omega$ for radial and $\pm\Omega$ for circumferential modes. Combining this with the shift of $\pm n\Omega$ obtained from changing the frame of reference, the natural circular frequencies of the rotating wheel in the inertial frame may be approximated as

$$\omega_n \approx \begin{cases} \omega_{n,0} \pm |n|\Omega & \text{(axial)} \\ \omega_{n,0} \pm (|n|-1)\Omega & \text{(radial)} \\ \omega_{n,0} \pm (|n|+1)\Omega & \text{(circumferential)} \end{cases}, \tag{37}$$

where $\omega_{n,0}$ is the natural circular frequency of the non-rotating wheel ($\Omega = 0$).

At higher values of n, the frequency shifts for the radial and circumferential modes become smaller, and these estimations can become less accurate. The approximate formulae are most accurate if modes have uncoupled vibration, e.g. for a flat disc, where radial modes have almost purely radial vibration (likewise the axial and circumferential modes). For the more complex wheel geometry, the frequency shifts of specific modes depend on the degree of coupling between different directions. Nevertheless, if the exact natural frequencies of the rotating wheels are required, the Eulerian or Lagrangian models should be used.

4.2 Inclusion of an axle in the wheelset model

Modelling a single wheel with a fixed hub is often preferred to a full wheelset, to reduce the number of degrees of freedom in the FE model and its calculation times [1]. The presence of the axle introduces coupling between the two wheels for $n = 0$, through axle torsion/extension, or for $n = \pm 1$, through axle bending [6]. This can alter the frequency shifts compared with the wheel alone constrained at the hub. At higher numbers of nodal diameters ($|n| \geq 2$), except for a few modes, the axle remains rigid and effectively decouples the two wheels in the frequency range of interest. Hence, the frequency shifts of the wheelset are identical to those of the single wheel shown in **Fig. 2**, but each mode exists as a doublet at the same natural frequency, in which either the left or the right wheel vibrates. Stress stiffening is excluded in these full wheelset calculations.

The frequency shifts of the wheelset modes with $n = 0$ and $n = \pm 1$ are shown in **Fig. 4**. Because of the coupling between the wheel and the axle vibration, modes cannot always be clearly distinguished as radial, circumferential, or axial. The modes with $n = 0$ do not split. Nevertheless, small changes in frequency (increase or decrease) with increasing speed are present due to gyroscopic and centrifugal effects. However, apart from a torsional mode that decreases by 20 Hz, the shift at 500 km/h is generally less than 1 Hz. For $n = \pm 1$, the frequency shifts are more widely distributed between $\pm\Omega/2\pi$.

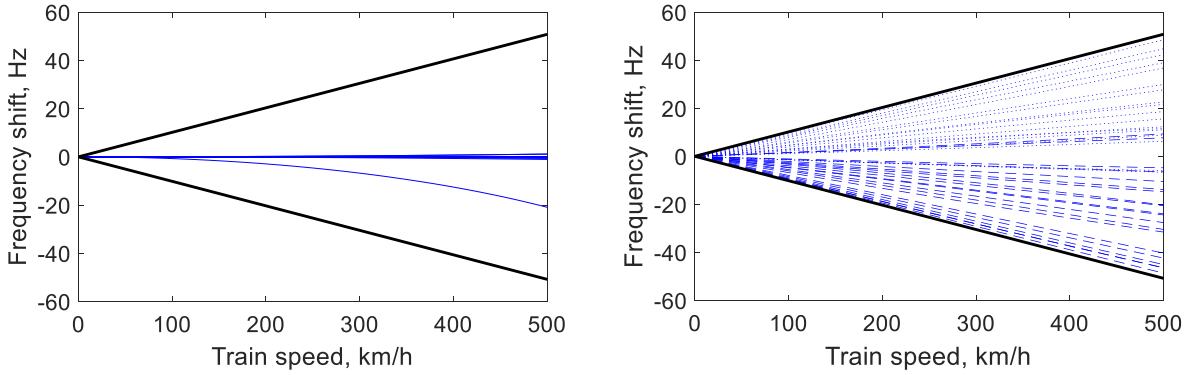

(a) (b)

Fig. 4 Frequency shift in the non-inertial frame of the modes from the rotating wheelset for train speeds up to 500 km/h and the harmonics (a) $n = 0$ and (b) $n = \pm 1$; —, standing wave (only for $n = 0$); – – –, forward rotating wave; · · ·, backward rotating wave; ▬, $\pm\Omega/2\pi$.

5 Vibration and rolling noise contribution of the rotating wheel

The wheel contribution to rolling noise is calculated in this section. Comparisons are made between wheel models that are non-rotating, rotating, or that implement rotation effects in an approximate way by means of a moving load. Unless otherwise stated, the wheel considered in the previous sections is investigated, which has a straight web. Frequencies from 10 Hz to 10 kHz are considered, to obtain results up to the 8 kHz one-third octave band. Train speeds from 10 to 500 km/h are included in the calculations. Although rolling noise may no longer be the dominant noise source for train speeds above 350 km/h [1], higher speeds are included for completeness and to show continuing trends.

5.1 Rolling noise from the rotating wheel

The vertical mobilities used to determine the contact forces for roughness excitation are compared in **Fig. 5**. The lateral and vertical/lateral cross mobilities are not shown for brevity, since the trends are identical. The wheel mobility obtained with the Eulerian model at 350 km/h is shown together with a continuously supported track model and the contact mobility at the driving point. Harmonics up to $n = \pm 10$ were considered to include resonances up to 10 kHz. The rigid body motion of the wheelset is added to the wheel mobility, calculated from the FE model with the fixed hub, as an approximation of the full wheelset dynamics.

In the wheel mobility, in the Eulerian frame, resonances split into two peaks according to the frequency separations discussed in Section 4. This is different from the non-rotating wheel, where the two rotating waves add up at the same frequency forming a single resonance peak. When adopting the moving load to approximate the rotation, which neglects the gyroscopic and centrifugal effects, a separation of exactly $\pm n\Omega/2\pi$ compared with the non-rotating wheel would be seen [7].

The Timoshenko beam model used for the rail neglects cross-section deformation, and the effects of discrete supports are also neglected here. However, for the comparison between the sound power radiated by the different wheel models, this track model is considered to be sufficient as it captures the main effects that the rail has in defining the contact force and hence the wheel vibration response [1].

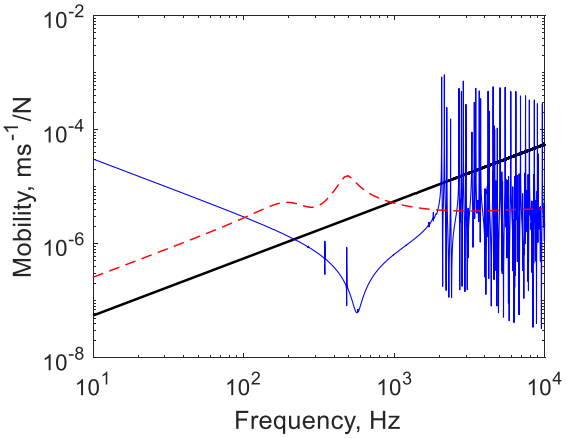

Fig. 5 Comparison of the magnitude of vertical driving point mobilities used in the interaction model; —, rotating wheelset at a train speed of 350 km/h (Eulerian model); – – –, continuously supported track; ▬, wheel/rail contact stiffness.

The sound power level (SWL) of the wheel is shown in **Fig. 6** in one-third octave bands for the train speeds 80, 160, and 350 km/h. The result for the non-rotating wheel is compared with the rotating wheel calculated using the Eulerian model (without stress stiffening). With increasing train speed, the SWL increases due to the higher roughness amplitude at a given frequency.

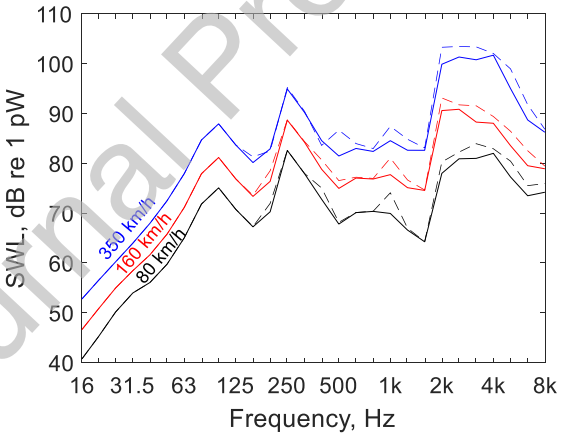

Fig. 6 Sound power level radiated by the wheel for train speeds of 80, 160, and 350 km/h comparing different wheel models; —, non-rotating wheel; – – –, rotating wheel (Eulerian).

The relative differences in SWL between the non-rotating and Eulerian wheel model can be seen in **Fig. 7**(a), including for the maximum speed of 500 km/h. Up to 125 Hz the models are in good agreement. Differences of around ± 2 dB occur up to 400 Hz. Above this frequency, the non-rotating model underestimates the Eulerian model by up to 6 dB. However, above 2 kHz, where the wheel has many resonances and usually produces most noise, the difference reduces to 2-4 dB, depending on the train speed. Generally, at higher

speeds the differences are larger. For the speeds considered, the moving load approximation has differences of less than 1 dB compared with the Eulerian model in all frequency bands, except for 2 dB in the 2 kHz band at 500 km/h, see **Fig. 7**(b).

The underestimation when using the non-rotating wheel is due to the wheel response which is determined from the circumferential mean square velocity after combining the two responses of harmonics $\pm n$ coherently as they combine to form a standing wave. In most frequency bands, this response is smaller than for the rotating wheels. The non-rotating wheelset model is not generally adopted in rolling noise calculations. Instead, the wheel rotation effects are commonly approximated by means of a load moving around the wheel circumference; this is implemented in TWINS [7]. The moving load model can approximate the SWL of the rotating wheel much better than the non-rotating wheel at regular train speeds. The small differences compared with the Eulerian model are due to the additional frequency separation and changes in amplitude of the resonances caused by the gyroscopic and centrifugal effects.

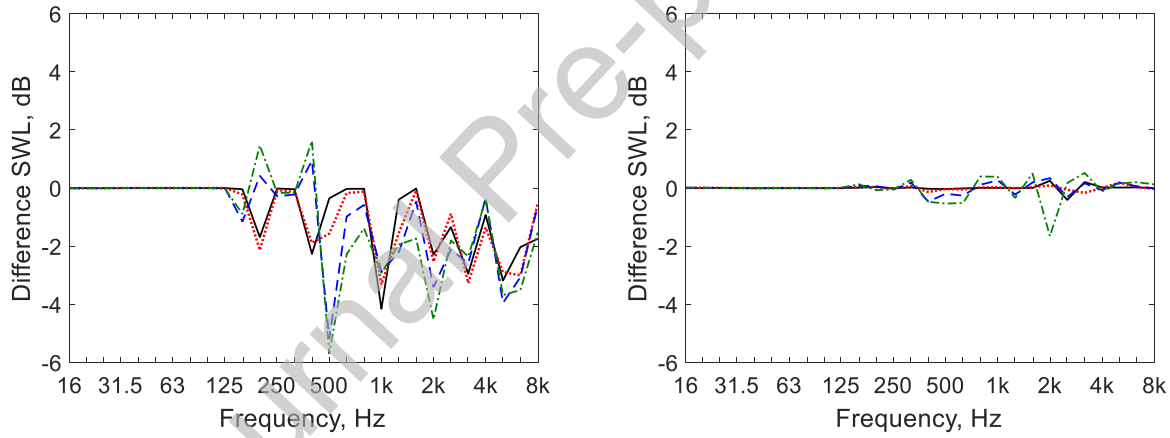

(a) (b)

Fig. 7 Difference in SWL comparing the Eulerian model with (a) the non-rotating wheel model and (b) the approximation with the moving load for different train speeds; —, 80 km/h; · · ·, 160 km/h; – – –, 350 km/h; – · –, 500 km/h

To formulate general conclusions about the effect of wheel rotation on the sound radiation from the wheel, calculations have been performed to cover train speeds from 10 to 500 km/h. Taking the Eulerian model (without stress-stiffening effects) as a reference, the relative differences of the overall A-weighted SWL of the wheel are shown in **Fig. 8** for different modelling approaches. These are (i) a non-rotating wheel, (ii) a moving load and (iii) the Eulerian approach that includes stress-stiffening effects. Results are shown for two different

wheel types, one with a straight web (as above) and another one with a curved web. Positive values mean an overestimation with respect to the reference Eulerian model.

At lower speeds, neglecting the rotation causes the overall A-weighted SWL to be underestimated by 1-2 dB. Above 100 km/h, the differences increase to almost 3 dB for the wheel with the curved web but remain below 2.5 dB for the wheel with straight web. That is due to the increase of the SWL in the frequency bands above 1.6 kHz, which contribute more significantly to the overall SWL at higher train speeds, see e.g. **Fig. 6**.

If the stress-stiffening effect is included in the Eulerian model, the differences are smaller than 0.2 dB, as the consequent frequency shifts remain small. To simplify the calculations, the stress-stiffening effect may therefore be neglected in rolling noise calculations.

The moving load model of the rotating wheel gives a good approximation to the Eulerian model, with differences of less than 0.2 dB for the straight web; for the curved web the differences remain less than 0.3 dB below 400 km/h, increasing to 0.6 dB at 500 km/h. Small variations are seen over speed as there are slight changes in the frequency separation and amplitude of the resonances. The differences in individual one-third octave bands can be as much as 2 dB. Other wheel designs will have slightly different results, but the general conclusions inferred from these examples will also hold for other common wheel geometries.

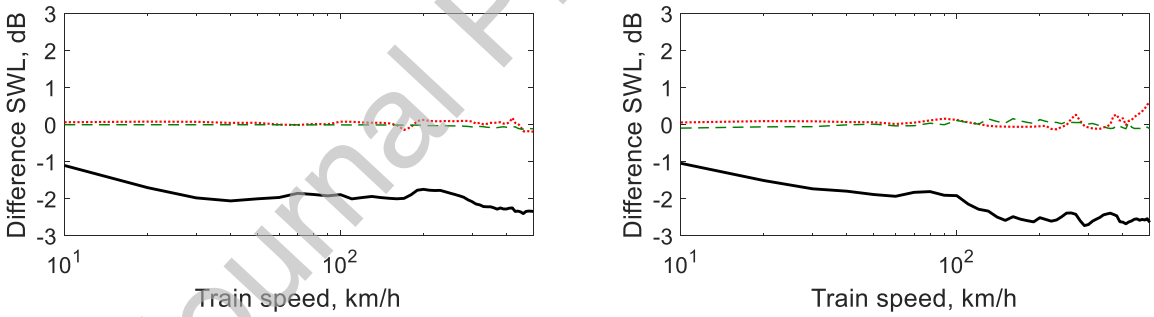

(a) (b)

Fig. 8 Difference in total A-weighted sound power level for the wheel models with (a) straight web and (b) curved web, relative to the Eulerian model for different train speeds; ▬, non-rotating wheel; · · ·, rotating wheel (moving load); – – –, rotating wheel (Eulerian with stress stiffening).

These differences are smaller than other sources of uncertainty, such as the measurements of roughness within the running band [31], suggesting that effects due to rotation other than the moving load can be safely neglected in rolling noise modelling. The non-rotating wheel shows larger differences of up to 3 dB in the overall A-weighted SWL. Its use should be restricted to comparisons with measurements using experimental modal analysis, to obtain modal parameters and update the FE model accordingly.

5.2 Comparison of the rotating wheel with the full wheelset

In the previous calculations, the response of the wheelset was approximated by adding rigid body modes to a model of a single wheel fixed at the hub (rigid axle). To investigate the effect of this approximation, calculations with the Eulerian model were repeated using a model that includes the geometry of the entire wheelset. The contribution of the axle vibration to the sound radiation is not accounted for, but this was found by Cheng et al. [21] to be negligible compared with the contribution of the wheels at frequencies above 2 kHz. Thus, the approximate wheel radiation efficiencies from [30] are again used.

In **Fig. 9**, the SWL of the wheel with rigid axle (as in Section 5.1) is compared with the full wheelset with flexible axle for three speeds, 80, 160 and 350 km/h. Although more modes exist in the full wheelset for $n = 0$ and $n = \pm 1$, the effect on the sound radiation is only about ± 1 dB in the frequency bands above 1 kHz, where the wheel contribution normally dominates the rolling noise [1]. In the bands between 80 Hz and 1 kHz differences of up to 6 dB are present, since several wheelset modes exist in this frequency range that are not included in the wheel-only model. The differences also tend to be larger at higher train speeds. However, below 1 kHz the track is usually the dominant noise source [1].

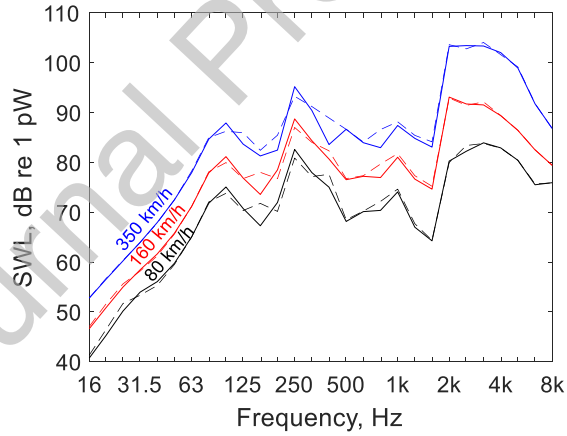

Fig. 9 SWL predicted with the Eulerian model of a rotating wheel and a wheelset for train speeds of 80, 160, and 350 km/h; —, wheel only; – – –, full wheelset.

The overall wheel contribution is mostly dominated by the frequency bands above 1.6 kHz, where the differences between the two modelling approaches are almost negligible. In terms of the overall A-weighted SWL, therefore, the noise from the full rotating wheelset is increased by less than 0.5 dB compared with the rotating wheel model in the prediction, see **Fig. 10**.

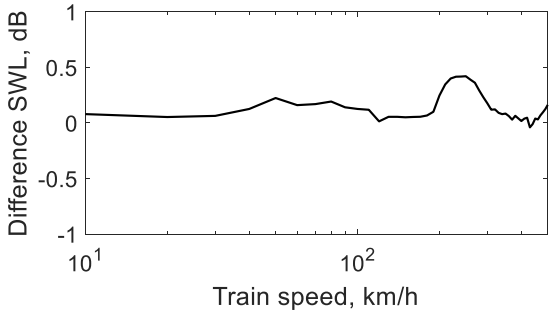

Fig. 10 Difference in SWL of a rotating wheel and a full wheelset modelled with the Eulerian model for train speeds from 10-500 km/h.

It is concluded that using a wheel model constrained at the hub and with added rigid body motion in rolling noise predictions is not disadvantageous compared with the full wheelset model.

5.3 Comparison with TWINS calculations

In the TWINS model, the wheel response is obtained in a non-inertial frame of reference. This allows direct comparison with wheel vibration measurements performed with accelerometers mounted on the wheel web [7]. However, to calculate the sound radiation it is more appropriate to evaluate the vibration velocity of the wheel, and the subsequent radiation of sound, in an inertial frame of reference. To evaluate the difference between the two approaches, the calculations were repeated with a TWINS model. For consistency with the TWINS calculation, the results obtained using the current model are done by approximating the rotation effects with a moving load.

The axial and radial wheel velocity responses obtained in both frames are shown in **Fig. 11** for train speeds of 80 and 350 km/h. The axial velocity is obtained at the centre of the web and the radial velocity at the nominal contact point. Differences in some frequency bands can be as large as 8 dB, especially below 1.6 kHz, and appear to be larger for the higher speed. Above 1.6 kHz, the differences reduce to about 2 dB. Because the frequencies of the resonances are different in the two reference frames, they can appear in different one-third octave bands, which causes the difference in the velocity levels.

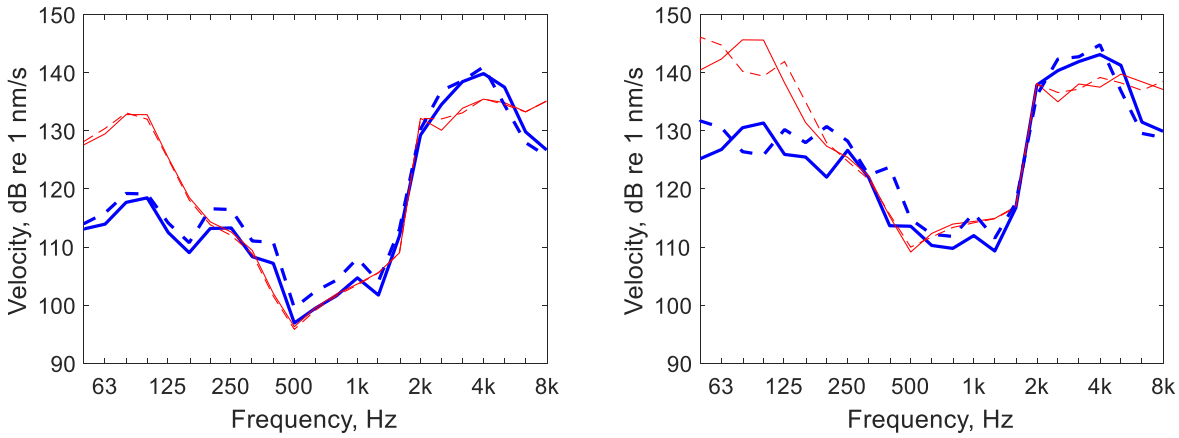

Fig. 11 Comparing the wheel response at the contact point (radial) and the web (axial) in the two reference frames for a train speed of (a) 80 km/h and (b) 350 km/h; **▬**, axial in inertial frame; **- - -**, axial in non-inertial frame; —, radial in inertial frame; – – –, radial in non-inertial frame.

The overall A-weighted SWL for the range of speeds considered in this study can be seen in **Fig. 12**. A positive value means an increase compared with the inertial frame that is adopted in this work. It shows that the effect of changing reference frame on the overall A-weighted SWL is small, with differences up to about 0.5 dB.

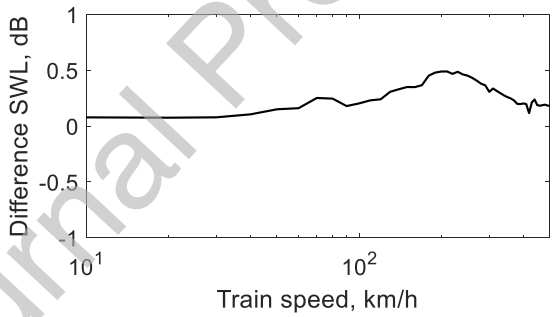

Fig. 12 Difference in SWL between calculations of the wheel response and consequent sound radiation in an inertial and in a non-inertial frame.

The overall A-weighted SWL is not significantly affected by whether the inertial frame (current paper) or the non-inertial frame (TWINS) is used to calculate the wheel response, but there are fluctuations in some frequency bands.

6 Conclusions

The effect of the rotation on predicted vibration and radiated sound from the train wheel in rolling noise has been investigated. Different wheel models are compared in the calculations. The effects of the rotation on the wheel modal frequencies were obtained from a Lagrangian model. An Eulerian model was used to determine the wheelset mobility and predict the rolling noise based on the TWINS approach.

When the rotation is included, modes that exist as standing waves in the non-rotating wheel become forward and backward rotating waves, with diverging frequencies that separate with increasing speed. The frequency split depends on the mode shapes and can vary for different wheel types. In general, axial wheel modes are barely affected by the rotation (in the Lagrangian frame), whereas radial and circumferential modes have a larger frequency split, up to almost $\pm\Omega/2\pi$. The reason for the divergence is the gyroscopic effect due to Coriolis forces, while stress stiffening or spin softening that either increase or decrease the modal frequency have a negligible effect at normal train speeds.

In the calculated rolling noise from the wheel, the differences in the SWL between the non-rotating wheel and the model including all effects of the rotation can be as large as 6 dB in some frequency bands. The overall A-weighted SWL is underestimated by up to 3 dB when using the non-rotating wheel. The moving load approximation, however, whilst neglecting gyroscopic and centrifugal effects (spin softening and stress stiffening), gives differences of only up to 1 dB in some frequency bands for conventional train speeds. The overall A-weighted SWL has differences of less than 0.3 dB for train speeds below 400 km/h, which is small compared with other sources of uncertainty in rolling noise predictions.

When modelling the wheelset by a single wheel with a constrained hub and adding the rigid body motion, differences can be expected of up to 6 dB in some frequency bands below 1 kHz compared with a full wheelset model that includes the axle. However, the difference in overall A-weighted SWL is only about 0.5 dB. Similar differences are found if the wheel response and sound radiation are calculated in a non-inertial frame as in TWINS, rather than an inertial frame as in the model presented in this paper.

Acknowledgement

The fourth author acknowledges the financial support through the grant PID2020-118013RB-C21 funded by MCIN/AEI/10.13039/501100011033.

Data availability statement

Data published in this paper are openly available from the University of Southampton repository (TBD after manuscript was accepted).

Appendix A– Element matrices of the rotating axisymmetric FE model

In this appendix the element matrices of the axisymmetric FE rotor model are provided. The element mass, gyroscopic and centrifugal matrices and the centrifugal force vector in the expression of kinetic energy, see Eq. (9), are defined as

$$\mathbf{m}^e = 2\pi \iint_{A^e} r\rho \mathbf{N}^{e\mathrm{T}} \mathbf{N}^e \,\mathrm{d}r\mathrm{d}z, \tag{A.1}$$

$$\mathbf{g}^e = 2\pi \iint_{A^e} r\rho \mathbf{N}^{e\mathrm{T}} \mathbf{J} \mathbf{N}^e \,\mathrm{d}r\mathrm{d}z, \tag{A.2}$$

$$\mathbf{b}^e = 2\pi \iint_{A^e} r\rho \mathbf{N}^{e\mathrm{T}} \mathbf{E} \mathbf{N}^e \,\mathrm{d}r\mathrm{d}z, \tag{A.3}$$

$$\mathbf{c}_0^e = 2\pi \iint_{A^e} r^2\rho \mathbf{N}^{e\mathrm{T}} \begin{Bmatrix} 1 \\ 0 \\ 0 \end{Bmatrix} \mathrm{d}r\mathrm{d}z. \tag{A.4}$$

The surface integrals can be solved numerically using Gaussian Quadrature.

The stiffness matrices are derived from the strain energy in Eq. (10). To include centrifugal stress stiffening, geometric non-linearity has to be included, which requires Green strain with higher order terms [22]. Combining the six linear strain components [29] with the non-linear components [32] yields the strain vector $\boldsymbol{\varepsilon} = (\varepsilon_r, \varepsilon_\theta, \varepsilon_z, \gamma_{zr}, \gamma_{r\theta}, \gamma_{\theta z})^{\mathrm{T}}$ as

$$\boldsymbol{\varepsilon} = \boldsymbol{\varepsilon}_l + \boldsymbol{\varepsilon}_{nl} = \begin{bmatrix} \frac{\partial u_r}{\partial r} \\ \frac{1}{r}\left(\frac{\partial u_\theta}{\partial \theta} + u_r\right) \\ \frac{\partial u_z}{\partial z} \\ \frac{\partial u_z}{\partial r} + \frac{\partial u_r}{\partial z} \\ \frac{1}{r}\frac{\partial u_r}{\partial \theta} + \frac{\partial u_\theta}{\partial r} - \frac{u_\theta}{r} \\ \frac{1}{r}\frac{\partial u_z}{\partial \theta} + \frac{\partial u_\theta}{\partial z} \end{bmatrix} + \begin{bmatrix} \frac{1}{2}\left[\left(\frac{\partial u_r}{\partial r}\right)^2 + \left(\frac{\partial u_\theta}{\partial r}\right)^2 + \left(\frac{\partial u_z}{\partial r}\right)^2\right] \\ \frac{1}{2r^2}\left[\left(\frac{\partial u_\theta}{\partial \theta} + u_r\right)^2 + \left(\frac{1}{r}\frac{\partial u_r}{\partial \theta} - u_\theta\right)^2 + \left(\frac{\partial u_z}{\partial \theta}\right)^2\right] \\ \frac{1}{2}\left[\left(\frac{\partial u_r}{\partial z}\right)^2 + \left(\frac{\partial u_\theta}{\partial z}\right)^2 + \left(\frac{\partial u_z}{\partial z}\right)^2\right] \\ \frac{\partial u_r}{\partial r}\frac{\partial u_r}{\partial z} + \frac{\partial u_\theta}{\partial r}\frac{\partial u_\theta}{\partial z} + \frac{\partial u_z}{\partial r}\frac{\partial u_z}{\partial z} \\ \frac{1}{r}\left[\frac{\partial u_r}{\partial r}\left(\frac{\partial u_r}{\partial \theta} - u_\theta\right) + \frac{\partial u_\theta}{\partial r}\left(\frac{\partial u_\theta}{\partial \theta} + u\right) + \frac{\partial u_z}{\partial r}\frac{\partial u_z}{\partial \theta}\right] \\ \frac{1}{r}\left[\frac{\partial u_\theta}{\partial z}\left(\frac{\partial u_\theta}{\partial \theta} + u_r\right) + \frac{\partial u_r}{\partial z}\left(\frac{\partial u_r}{\partial \theta} - u_\theta\right) + \frac{\partial u_z}{\partial z}\frac{\partial u_z}{\partial \theta}\right] \end{bmatrix}, \tag{A.5}$$

where ε_i represents the strains in the i-th direction and γ_{ij} the shear strains between the i-th and j-th directions. Without pre-stress ($\boldsymbol{\sigma}_0 = \mathbf{0}$), the second term in Eq. (10) vanishes and the standard element stiffness matrices in the axisymmetric approach are obtained as

$$\mathbf{k}_0^e = 2\pi \iint_{A^e} r\mathbf{B}_0^{e\mathrm{T}} \mathbf{D} \mathbf{B}_0^e \,\mathrm{d}r\mathrm{d}z, \tag{A.6}$$

$$\mathbf{k}_1^e = 2\pi \iint_{A^e} r\left(\mathbf{B}_0^{e\mathrm{T}} \mathbf{D} \mathbf{B}_1^e + (-\mathbf{B}_1^e)^{\mathrm{T}} \mathbf{D} \mathbf{B}_0^e\right) \mathrm{d}r\mathrm{d}z, \tag{A.7}$$

$$\mathbf{k}_2^e = 2\pi \iint_{A^e} r(-\mathbf{B}_1^e)^{\mathrm{T}} \mathbf{D} \mathbf{B}_1^e \,\mathrm{d}r\mathrm{d}z, \tag{A.8}$$

where $\mathbf{B}_0^e$ and $\mathbf{B}_1^e$ are the element strain-displacement matrices of the linear strains $\boldsymbol{\varepsilon}_l$ defined as [22, 29]

$$\mathbf{B}_0^e = \begin{bmatrix} \frac{\partial}{\partial r} & 0 & 0 \\ \frac{1}{r} & 0 & 0 \\ 0 & 0 & \frac{\partial}{\partial z} \\ \frac{\partial}{\partial z} & 0 & \frac{\partial}{\partial r} \\ 0 & \left(\frac{\partial}{\partial r} - \frac{1}{r}\right) & 0 \\ 0 & \frac{\partial}{\partial z} & 0 \end{bmatrix} \mathbf{N}^e \quad \text{and} \quad \mathbf{B}_1^e = \frac{1}{r} \begin{bmatrix} 0 & 0 & 0 \\ 0 & 1 & 0 \\ 0 & 0 & 0 \\ 0 & 0 & 0 \\ 1 & 0 & 0 \\ 0 & 0 & 1 \end{bmatrix} \mathbf{N}^e, \tag{A.9}$$

and the matrix of elastic moduli $\mathbf{D}$ is

$$\mathbf{D} = \frac{E}{(1+\nu)(1-2\nu)} \begin{bmatrix} (1-\nu) & \nu & \nu & 0 & 0 & 0 \\ \nu & (1-\nu) & \nu & 0 & 0 & 0 \\ \nu & \nu & (1-\nu) & 0 & 0 & 0 \\ 0 & 0 & 0 & \left(\frac{1}{2}-\nu\right) & 0 & 0 \\ 0 & 0 & 0 & 0 & \left(\frac{1}{2}-\nu\right) & 0 \\ 0 & 0 & 0 & 0 & 0 & \left(\frac{1}{2}-\nu\right) \end{bmatrix}, \tag{A.10}$$

where E is the Young's modulus and ν the Poisson's ratio.

To include the pre-stress, geometric non-linearity needs to be included using the non-linear strains $\boldsymbol{\varepsilon}_{nl}$. After evaluating the elemental pre-stress from the static displacement field $\bar{\mathbf{u}}_0$ at the Gaussian integration points as

$$\boldsymbol{\sigma}_0^e(\bar{\mathbf{u}}_0) = \mathbf{D}\mathbf{B}_0^e\bar{\mathbf{u}}_0^e, \tag{A.11}$$

the element geometric stiffness matrix can be integrated as

$$\mathbf{k}_g^e = 2\pi \iint_{A^e} r\mathbf{B}_2^{e\mathrm{T}}\mathbf{S}^e\mathbf{B}_2^e \,\mathrm{d}r\mathrm{d}z, \tag{A.12}$$

where $\mathbf{B}_2^e$ adopts the non-linear strain components, and $\mathbf{S}^e$ contains the pre-stresses within the element obtained from Eq. (A.11). The strain-displacement matrix $\mathbf{B}_2^e$ is given by

$$\mathbf{B}_2^e = \begin{bmatrix} \frac{\partial}{\partial r} & 0 & 0 \\ \frac{n}{r} & -\frac{1}{r} & 0 \\ \frac{\partial}{\partial z} & 0 & 0 \\ 0 & \frac{\partial}{\partial r} & 0 \\ \frac{1}{r} & \frac{n}{r} & 0 \\ 0 & \frac{\partial}{\partial z} & 0 \\ 0 & 0 & \frac{\partial}{\partial r} \\ 0 & 0 & \frac{n}{r} \\ 0 & 0 & \frac{\partial}{\partial z} \end{bmatrix} \mathbf{N}^e, \tag{A.13}$$

and the elemental stress and shear stress components in the three principal directions, from Eq. (A.14), are re-ordered as follows [22]

$$\mathbf{S}^e = \begin{bmatrix} \mathbf{s}^e & \mathbf{0} & \mathbf{0} \\ \mathbf{0} & \mathbf{s}^e & \mathbf{0} \\ \mathbf{0} & \mathbf{0} & \mathbf{s}^e \end{bmatrix}, \tag{A.15}$$

with

$$\mathbf{s}^e = \begin{bmatrix} \sigma_r & \tau_{\theta r} & \tau_{zr} \\ \sigma_{r\theta} & \sigma_\theta & \tau_{z\theta} \\ \tau_{rz} & \tau_{\theta z} & \sigma_z \end{bmatrix}, \tag{A.16}$$

where σ_i represents the stress components in the i-th direction and τ_{ij} the shear stresses between the i-th and j-th directions. Due to the non-linear strains in the formulation of geometric stiffening, unrealistic results can occur at rigid body modes if an unconstrained structure is modelled [33].

References

[1] D. J. Thompson, *Railway noise and vibration: mechanisms, modelling and means of control*, 1st ed. Amsterdam: Elsevier, 2009.

[2] D. J. Thompson, B. Hemsworth, and N. Vincent, "Experimental validation of the TWINS prediction program for rolling noise, part 1: description of the model and method," *Journal of Sound and Vibration*, vol. 193, no. 1, pp. 123-135, 1996, doi: https://doi.org/10.1006/jsvi.1996.0252.

[3] D. J. Thompson, P. Fodiman, and H. Mahé, "Experimental validation of the TWINS prediction program for rolling noise, part 2: results," *Journal of Sound and Vibration*, vol. 193, no. 1, pp. 137-147, 1996, doi: https://doi.org/10.1006/jsvi.1996.0253.

[4] P. J. Remington, "Wheel/rail noise—part I: characterization of the wheel/rail dynamic system," *Journal of Sound and Vibration*, vol. 46, no. 3, pp. 359-379, 1976, doi: https://doi.org/10.1016/0022-460X(76)90861-0.

[5] P. J. Remington, "Wheel/rail noise—part IV: rolling noise," *Journal of Sound and Vibration*, vol. 46, no. 3, pp. 419-436, 1976, doi: https://doi.org/10.1016/0022-460X(76)90864-6.

[6] D. J. Thompson, "Wheel Rail Noise Generation, part II: Wheel Vibration," *Journal of Sound and Vibration*, vol. 161, no. 3, pp. 401-419, 1993, doi: https://doi.org/10.1006/jsvi.1993.1083.

[7] D. J. Thompson, "Wheel Rail Noise Generation, part V: Inclusion of Wheel Rotation," *Journal of Sound and Vibration*, vol. 161, no. 3, pp. 467-482, 1993, doi: https://doi.org/10.1006/jsvi.1993.1086.

[8] J. Fayos, L. Baeza, F. D. Denia, and J. E. Tarancon, "An Eulerian coordinate-based method for analysing the structural vibrations of a solid of revolution rotating about its main axis," *Journal of Sound and Vibration*, vol. 306, no. 3-5, pp. 618-635, 2007, doi: https://doi.org/10.1016/j.jsv.2007.05.051.

[9] L. Baeza, P. Vila, G. Xie, and S. D. Iwnicki, "Prediction of rail corrugation using a rotating flexible wheelset coupled with a flexible track model and a non-Hertzian/non-steady contact model," *Journal of Sound and Vibration*, vol. 330, no. 18-19, pp. 4493-4507, 2011, doi: https://doi.org/10.1016/j.jsv.2011.03.032.

[10] J. Martínez-Casas, L. Mazzola, L. Baeza, and S. Bruni, "Numerical estimation of stresses in railway axles using a train–track interaction model," *International Journal of Fatigue*, vol. 47, pp. 18-30, 2013, doi: https://doi.org/10.1016/j.ijfatigue.2012.07.006.

[11] J. Martínez-Casas, J. Giner-Navarro, L. Baeza, and F. D. Denia, "Improved railway wheelset–track interaction model in the high-frequency domain," *Journal of Computational and Applied Mathematics*, vol. 309, pp. 642-653, 2017, doi: https://doi.org/10.1016/j.cam.2016.04.034.

[12] A. Pieringer, L. Baeza, and W. Kropp, "Modelling of railway curve squeal including effects of wheel rotation," in: J.C.O. Nielsen, et al. *Noise and Vibration Mitigation for Rail Transportation Systems. Notes on Numerical Fluid Mechanics and Multidisciplinary Design*, vol 126, pp. 417-424. Springer, Berlin, Heidelberg, 2015, https://doi.org/10.1007/978-3-662-44832-8_50.

[13] V. T. Andrés, J. Martínez-Casas, F. D. Denia, and D. J. Thompson, "A model of a rotating railway wheel for the prediction of sound radiation," *Journal of Sound and Vibration*, vol. 553, p. 117667, 2023, doi: https://doi.org/10.1016/j.jsv.2023.117667.

[14] L. Baeza, J. Giner-Navarro, D. J. Thompson, and J. Monterde, "Eulerian models of the rotating flexible wheelset for high frequency railway dynamics," *Journal of Sound and Vibration*, vol. 449, pp. 300-314, 2019, doi: https://doi.org/10.1016/j.jsv.2019.03.002.

[15] L. Baeza, J. Giner-Navarro, and D. J. Thompson, "Reply to "Discussion on 'Eulerian models of the rotating flexible wheelset for high frequency railway dynamics' [J. Sound Vib. 449 (2019) 300-314]"," *Journal of Sound and Vibration*, vol. 489, p. 115665, 2020, doi: https://doi.org/10.1016/j.jsv.2020.115665.

[16] L. Baeza, J. Giner-Navarro, C. Knuth, and D. J. Thompson, "Comprehensive model of a rotating flexible wheelset for high-frequency railway dynamics," *Mechanical Systems and Signal Processing*, vol. 200, p. 110592, 2023, doi: https://doi.org/10.1016/j.ymssp.2023.110592.

[17] X. Sheng, Y. X. Liu, and X. Zhou, "The response of a high-speed train wheel to a harmonic wheel-rail force," *Journal of Physics: Conference Series*, vol. 744, p. 012145, 2016, doi: https://doi.org/10.1088/1742-6596/744/1/012145.

[18] X. Z. Sheng, G. Cheng, and D. J. Thompson, "Modelling wheel/rail rolling noise for a high-speed train running along an infinitely long periodic slab track," *Journal of the Acoustical Society of America*, vol. 148, no. 1, pp. 174-190, 2020, doi: https://doi.org/10.1121/10.0001566.

[19] S. Zhang, G. Cheng, X. Sheng, and D. J. Thompson, "Dynamic wheel-rail interaction at high speed based on time-domain moving Green's functions," *Journal of Sound and Vibration*, vol. 488, 2020, doi: https://doi.org/10.1016/j.jsv.2020.115632.

[20] T. Zhong, G. Chen, X. Sheng, X. Zhan, L. Zhou, and J. Kai, "Vibration and sound radiation of a rotating train wheel subject to a vertical harmonic wheel–rail force," *Journal of Modern Transportation*, vol. 26, no. 2, pp. 81-95, 2018, doi: https://doi.org/10.1007/s40534-017-0154-6.

[21] G. Cheng, Y. He, J. Han, X. Sheng, and D. J. Thompson, "An investigation into the effects of modelling assumptions on sound power radiated froma high-speed train wheelset," *Journal of Sound and Vibration*, vol. 495, p. 115910, 2021, doi: https://doi.org/10.1016/j.jsv.2020.115910.

[22] R. D. Cook, D. S. Malkus, M. E. Plesha, and R. J. Witt, *Concepts and Applications of Finite Element Analysis*, 4th ed. Hoboken: Wiley, 2001.

[23] G. Genta, *Dynamics of Rotating Systems*, 1st ed. (Mechanical Engineering Series). New York: Springer, 2005.

[24] M. I. Friswell, J. E. T. Penny, S. D. Garvey, and A. W. Lees, *Dynamics of Rotating Machines*, 1st ed. Cambridge University Press, 2010.

[25] D. J. Thompson, "Wheel Rail Noise Generation, part III: Rail Vibration," *Journal of Sound and Vibration*, vol. 161, no. 3, pp. 421-446, 1993, doi: https://doi.org/10.1006/jsvi.1993.1084.

[26] D. J. Thompson, "Wheel Rail Noise Generation, part IV: Contact Zone and Results," *Journal of Sound and Vibration*, vol. 161, no. 3, pp. 447-466, 1993, doi: https://doi.org/10.1006/jsvi.1993.1085.

[27] *ISO 3095:2013 Acoustics – Railway applications – Measurement of noise emitted by rail-bound vehicles*, International Organisation for Standardization, Geneva.

[28] P. Remington and J. Webb, "Estimation of wheel/rail interaction forces in the contact area due to roughness," *Journal of Sound and Vibration*, vol. 193, no. 1, pp. 83-102, 1996, doi: https://doi.org/10.1006/jsvi.1996.0249.

[29] M. Petyt, *Introduction to finite element vibration analysis*, 2nd ed. Cambridge: Cambridge University Press, 2010.

[30] D. J. Thompson and C. J. C. Jones, "Sound radiation from a vibrating railway wheel," *Journal of Sound and Vibration*, vol. 253, no. 2, pp. 401-419, 2002, doi: https://doi.org/10.1006/jsvi.2001.4061.

[31] G. Squicciarini, M. G. R. Toward, D. J. Thompson, and C. J. C. Jones, "Statistical Description of Wheel Roughness," in: J.C.O. Nielsen, et al. *Noise and Vibration*

Mitigation for Rail Transportation Systems. Notes on Numerical Fluid Mechanics and Multidisciplinary Design, vol 126, pp. 651-658. Springer, Berlin, Heidelberg, 2015, https://doi.org/10.1007/978-3-662-44832-8_77

[32] L. Hu and A. Palazzolo, "An Enhanced Axisymmetric Solid Element for Rotor Dynamic Model Improvement," *Journal of Vibration and Acoustics*, vol. 141, no. 5, 2019, doi: https://doi.org/10.1115/1.4043411.

[33] C. M. Nilsson, "Waveguide finite elements applied on a car tyre," Ph.D. thesis, KTH Royal Institute of Technology Stockholm, 2004.

CRediT author statement

Christopher Knuth: Conceptualization, Methodology, Software, Validation, Formal analysis, Investigation, Visualization, Writing – Original draft, Writing – Review & Editing. **Giacomo Squicciarini**: Project administration, Supervision, Conceptualization, Methodology, Software, Resources, Writing – Review & Editing. **David Thompson**: Supervision, Conceptualization, Methodology, Software, Writing – Review & Editing. **Luis Baeza**: Conceptualization, Methodology, Validation, Writing – Review & Editing.

Declaration of interests

☒ The authors declare that they have no known competing financial interests or personal relationships that could have appeared to influence the work reported in this paper.

☐The authors declare the following financial interests/personal relationships which may be considered as potential competing interests: